Design and first results of a Fourier Transform imaging spectrometer in the 3-5 μm range

Noura Matallah, Hervé Sauer, François Goudail, Jean-Claude Fontanella, Yann Ferrec, Jean Albert Taboury, Pierre Chavel

https://dx.doi.org/10.1117/12.895935

Design and first results of a Fourier Transform imaging spectrometer in the 3-5 µm range

Noura Matallah[a,b], Hervé Sauer*[a], François Goudail[a], Jean-Claude Fontanella[b], Yann Ferrec[c], Jean Taboury[a], Pierre Chavel[a]

[a] Laboratoire Charles Fabry, UMR 8501, Institut d'Optique, CNRS, Univ Paris Sud 11, 2 avenue Augustin Fresnel, 91127 Palaiseau cedex, France.

[b] Thales Optronique SA, 2 avenue Gay Lussac, 78990 Élancourt cedex, France.

[c] Office National d'Études et de Recherches Aérospatiales, Chemin de la Hunière, 91761 Palaiseau cedex, France.

ABSTRACT

An imaging spectrometer in the 3-5 µm wavelength range is presented. This wavelength range reveals important information about scenes such as gas or landmine detection, but the amount of light is usually low and signal to noise ratio is a real issue. We selected a Fourier transform (FT) configuration, expecting an advantage in signal to noise ratio in the presence of detector noise. Radiometric and noise models are summarized.

A Michelson interferometer with its mirrors replaced by twin mirrors arranged at right angles in a hollow roof was chosen for its nearly straight equidistant fringes localized at infinity. Because in such FT-based spectral imagers, the interferogram is acquired over the whole field of the camera while the scene of interest scans the path difference range, vignetting should be strongly limited while keeping the size of the interferometer as small as possible for manufacturability and cost reasons. The key point for that purpose is to put the entrance pupil of the imaging lens inside the interferometer and to make careful trade-offs between lens F number and angular field of view.

The resulting system has a spectral resolution of about 25cm^{-1} that fulfils the requirement for most targeted applications. Examples of absorption bands detection are shown.

Keywords: Spectral imaging, Optical systems design, Fourier transform spectroscopy, Medium Wavelength Infra Red

1. INTRODUCTION

Hyperspectral imaging is a very useful modality in remote sensing applications[1][2][3]. In particular, spectral imaging in the 3-5 µm wavelength range can bring important information for such applications as decamouflaging, gas or landmine detection. However, in this wavelength range, the amount of light is usually low, and signal to noise ratio is a real issue.

There are two main ways to build spectral imagers[4]: The first one uses a grating and a slit, and the spectral image is directly acquired line by line along the track of the carrier in a pushbroom mode. The second uses the principle of Fourier transform spectrometry. The interferogram of each point of the scene may be recorded as it moves through the field of view. The spectrum of the light coming from a particular point is then calculated by the Fourier Transform (FT) of its interferogram. Grating-based spectral imagers are usually easier to build and the data they provide are often easier to interpret. However, FT spectral imagers are usually considered to provide a better signal to noise ratio if the main source of noise comes from the detector.

Because signal to noise ratio is a real issue in the applications we envisage (target or gas detection in the 3-5 µm range), we chose a FT-based spectral imager concept using a Michelson interferometer with right angle hollow roof mirrors[5]. In section 2, we describe the principle of this type of imager. In section 3, we quantify the gain brought by this architecture over grating-based architectures and illustrate the results on a realistic application scenario. In section 4, we describe the optical design of a demonstrator that we have built, emphasizing the specific problems encountered and our solutions. Finally, in section 5, we present first spectra and spectral images obtained with this system.

* e-mail: herve.sauer@institutoptique.fr

Optical Design and Engineering IV, edited by Laurent Mazuray, Rolf Wartmann, Andrew Wood, Jean-Luc M. Tissot, Jeffrey M. Raynor, Proc. of SPIE Vol. 8167, 816715 · © 2011 SPIE · CCC code: 0277-786X/11/$18 · doi: 10.1117/12.895935

2. A STATIC FT SPECTRAL IMAGING SCHEME

Let us first consider the basic principle of a FT spectrometer. Incoming light, with the help of a two-beam interferometer, is split into two paths, which travel different paths and are then recombined. The recorded interferogram can be written as:

$$I(\delta) = t_{\text{int}} . \int_{\sigma_{\min}}^{\sigma_{\max}} B_\sigma(\sigma) . \frac{1+\cos(2\pi\delta\sigma)}{2} d\sigma \qquad (1)$$

where I is a number of photoelectrons or detected photons on a elementary detector, δ the optical path difference between the two interfering waves at that detector, σ the wavenumber, $B_\sigma(\sigma)$ the spectral detected photonic flux received by an elementary detector *in the absence of the interferometer* (in "detected photons" per second), $\sigma_{\min}$ and $\sigma_{\max}$ the wavenumber range of the sensor responsivity, and t_{int} the integration time. The spectral photonic flux $B_\sigma(\sigma)$ depends of the spectral photonic radiance of the observed scene point $L_{\sigma,sc}(\sigma)$ and of the instrument details through :

$$B_\sigma(\sigma) = G.\tau_{lens}.\eta.L_{\sigma,sc}(\sigma) \qquad (2)$$

where G is the geometrical étendue defined by the elementary detector surface and the lens numerical aperture, τ_{lens} the transmission of the lens and η the quantum efficiency of the detectors assumed to be constant over the useful spectral range (and zero elsewhere). The beam splitter is assumed to be perfect (i.e. transmission and reflection coefficients are ½ independently of the wavelength), and otherwise it is assumed that no light is lost in any of the two arms; the interference effects are taken into account in Eq.(1) by the ½(1+cos(2πδσ)) factor.

Let us now consider a static FT imager based on lateral shift Michelson interferometer (Fig.1). The interferometer is composed of two right-angled hollow roof mirror reflectors and a beamsplitter which separates the incoming rays. The rays on the two arms are shifted by a quantity t equal to twice the lateral shift between one roof mirror reflector and the image of the other through the beam splitter. At one point of the sensor, the path difference depends on that translation t and on the source point field angle θ in the following way:

$$\delta = t.\sin(\theta) + C \qquad (3)$$

where C is defined, for not too large $|\theta|$, as twice the axial displacement of one roof mirror reflector relative to the image of the other. For the sake of simplicity, C will be assumed to be zero (0 order fringe in the center of the field) in what follows.

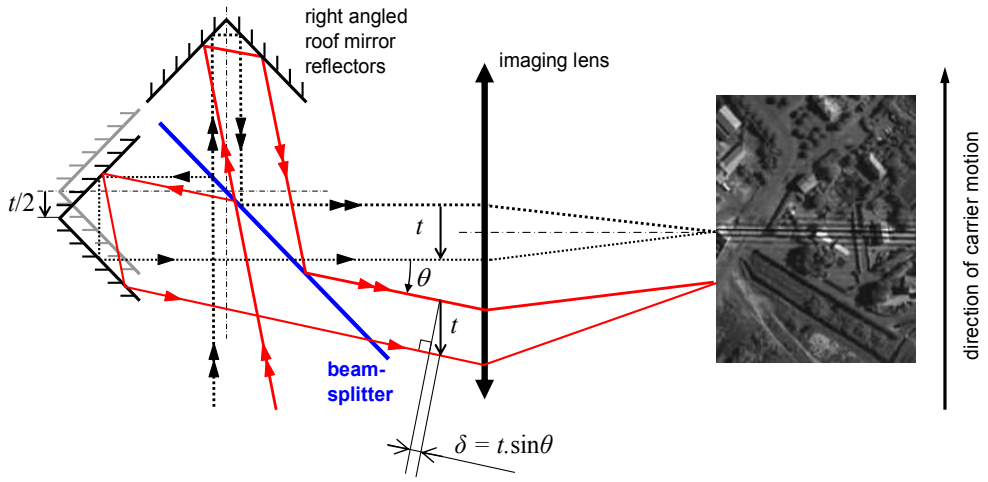

Figure 1: Schematic diagram of the roof mirrors Michelson interferometer used as an imaging static FT spectrometer. The direction of carrier motion is nearly perpendicular to fringes that stay still on a moving landscape image.

The system is designed so that the image of the observed scene and the fringe localization plane are superimposed in the sensor plane. To each point of the sensor plane thus corresponds a path difference δ. The rectilinear movement of the airborne sensor enables one to record the value of the interferogram for each point of the scene. The complete interferogram $I(\delta)$ of each point is acquired when this point has crossed the whole field of view of the sensor. The spectrum $B_\sigma(\sigma)$ of this point is finally estimated in the 3-5µm range by inverting Eq.(1), which essentially amounts to an inverse cosine transform. The main difficulties of this process are to register each image of the interferogram image stack sufficiently precisely and to calibrate the interferometer path differences to get the correct interferogram signal $I(\delta)$ for each scene point during the movement of its image along the sensor. Custom made software has been designed to perform those operations efficiently[6][7].

3. NOISE ADVANTAGE OF A FT SPECTRAL IMAGER WITH RESPECT TO GRATING BASED IMAGER

In this section, we illustrate the advantage, in some situations, of using a FT based spectrometer rather than a grating-based one. We firstly derive the expression of the signal to noise ratio for the estimation of the spectrum, and then illustrate this result on a realistic gas detection application.

3.1 Expression of the signal to noise ratio

Let us define the vector of the N sampled values $\vec{I}$ of the interferogram

$$I_i = I(\delta_i),\ \ \delta_i = i.\Delta\delta,\quad i \in \{0,\cdots,N-1\}, \tag{4}$$

with $\Delta\delta$ being the sampling interval. This constitutes the measurement actually done by the system.

The sampled values of the spectrum $\vec{B}$ are :

$$B_j = B_\sigma(\sigma_j),\ \ \sigma_j = j.\Delta\sigma,\quad j \in \{0,\cdots,N-1\},\ \text{with, e.g.,}\ \Delta\sigma = \frac{1}{2}\times\frac{1}{(N-½).\Delta\delta}. \tag{5}$$

The sampling step of the interferogram $\Delta\delta$ must be chosen in order that the Nyquist spatial frequency of the sampled interferogram, ½×1/$\Delta\delta$, be (slightly) greater than the upper bound $\sigma_{\max}$ of the detected light spectral range.

These two vectors $\vec{I}$ and $\vec{B}$ are related by a matrix transformation:

$$\vec{I} = \mathbf{M}.\vec{B} \tag{6}$$

where **M** is a $N \times N$ matrix. The matrix **M** depends on the spectral imager architecture.

For the static FT spectral imager (denoted by a $^{[TF]}$ superscript in what follows), this matrix is deduced from Eq.(1), (4) and (5):

$$\mathbf{M}^{[TF]}_{i,j} = t_{\text{int}}.\Delta\sigma.\frac{1+\cos\left(\frac{2\pi.i.j}{2N-1}\right)}{2},\quad (i,j) \in \{0,\cdots,N-1\}\times\{0,\cdots,N-1\}. \tag{7}$$

(Other slightly different definitions may have been taken for Eq.(5) and (7) relatively to the various possible definitions and conditionings of this pseudo discrete cosine transform, but we will not discuss that point here).

For a somewhat theoretical *direct* measure of the spectrum, for example with a kind of hypothetical grating, prism or grism based spectrometer (denoted by a $^{[Dir]}$ superscript below), the direct measurements can also be written in the same way as in Eq.(6), but with a diagonal matrix given by:

$$\mathbf{M}^{[Dir]} = t_{\text{int}}.\Delta\sigma.\mathbf{Id} \quad \text{where } \mathbf{Id} \text{ is the identity matrix.} \tag{8}$$

In practice, the measurements are affected by noise and Eq.(6) thus becomes:

$$\hat{\vec{I}} = \mathbf{M}.\vec{B} + \vec{n} \tag{9}$$

where $\vec{n}$ can be assumed to be a random vector with zero mean and covariance matrix defined by:

$$\mathbf{\Gamma}^n = \left\langle \vec{n}.\vec{n}^t \right\rangle \tag{10}$$

where $\langle\ \rangle$ denotes ensemble averaging and ^{t} transposition. The diagonal elements of the covariance matrix $\mathbf{\Gamma}^n$, denoted $v_k = \mathbf{\Gamma}^n_{k,k}$, represent the noise variance on each channel.

The spectrum $\vec{B}$ can be estimated by a plain matrix inversion:

$$\hat{\vec{B}} = \mathbf{M}^{-1}.\hat{\vec{I}} = \vec{B} + \vec{n'} \tag{11}$$

The noise on the estimated spectrum $\hat{\vec{B}}$ is given by the vector $\vec{n'} = \mathbf{M}^{-1}.\vec{n}$ and is characterized by the covariance matrix:

$$\mathbf{\Gamma}^{n'} = \left\langle \mathbf{M}^{-1}.\vec{n}\ .\ \vec{n}^t.\left(\mathbf{M}^{-1}\right)^t \right\rangle = \mathbf{M}^{-1}.\mathbf{\Gamma}^n.\left(\mathbf{M}^{-1}\right)^t \tag{12}$$

We will consider that the measurements can be perturbed by two types of noise. The first is the detector noise, which will be assumed to be white and Gaussian, so that its covariance matrix is diagonal. If we assume that the detector noise is the same far all the detectors, the covariance matrix can be written as:

$$\mathbf{\Gamma}^n = \gamma_n^2.\mathbf{Id} \tag{13}$$

where γ_n^2 represents the noise variance. This noise model can represent the readout noise and the dark noise; it is signal independent.

The second type of noise we consider is Poisson shot noise. It is white as well, with, thus, a diagonal covariance matrix also and its variance on detector *k* is equal to the value of the signal at the same detector measured as a number of detected photons, thus

$$Var[n_k] = I_k\ , \quad \mathbf{\Gamma}^n = \begin{bmatrix} I_0 & \ddots & 0 \\ & & \\ 0 & & I_{N-1} \end{bmatrix} \tag{14}$$

If these two types of noise are simultaneously present and statistically independent, their contributions add and the total noise variance $v_k = Var[n_k]$ on the measure is given by:

$$v_k = I_k + \gamma_n^2\ , \quad \text{with a diagonal covariance matrix } \mathbf{\Gamma}^n = \begin{bmatrix} v_0 & \ddots & 0 \\ & & \\ 0 & & v_{N-1} \end{bmatrix}. \tag{15}$$

The covariance matrix $\mathbf{\Gamma}^{n'}$ of the noise on the estimated spectrum has been given in Eq.(12). Its diagonal elements $u_k = \mathbf{\Gamma}^{n'}_{k,k}$ can be written:

$$u_k = \sum_{l=0}^{N-1} v_l.(m_{k,l})^2 \tag{16}$$

where $m_{k,l} = \left[\mathbf{M}^{-1}\right]_{k,l}$ with $(k,l) \in \{0,\cdots,N-1\} \times \{0,\cdots,N-1\}$.

The SNR on the estimator $\hat{B}_k$ of the spectrum can be defined by the ratio of the B_k value to the standard deviation of the noise on that estimated value:

$$SNR_k = \frac{B_k}{\sqrt{Var\left[\hat{B}_k\right]}} = \frac{B_k}{\sqrt{u_k}} \tag{17}$$

Let us consider the case of a direct measure of the spectrum. Considering equations Eq.(8) and Eq.(17), the SNR for each spectral element can be defined by:

$$SNR_k^{[Dir]} = \frac{B_\sigma(\sigma_k)}{\sqrt{u_k^{[Dir]}}} = \frac{t_{\text{int}}.\Delta\sigma.B_\sigma(\sigma_k)}{\sqrt{v_k^{[Dir]}}} = \frac{t_{\text{int}}.\Delta\sigma.B_\sigma(\sigma_k)}{\sqrt{\gamma_n^2 + t_{\text{int}}.\Delta\sigma.B_\sigma(\sigma_k)}} \tag{18}$$

where $k \in \{0,\cdots,N-1\}$. It can however be noted that this expression is relevant for only $\sim N\times(\sigma_{max}-\sigma_{min})/\sigma_{max}$ points when σ_k is in the useful $[\sigma_{\min}, \sigma_{\max}]$ spectral range. This could in practice relax the number of detectors required for the sensor for this direct measurement case.

In the FT case, reference [6] has established that the $SNR^{[TF]}$ can be expressed as :

$$SNR_k^{[TF]} = \frac{t_{\text{int}}.\Delta\sigma.B_\sigma(\sigma_k)}{\sqrt{\frac{8.\gamma_n^2}{N} + \frac{4}{N}.\sum_{k=0}^{N-1} t_{\text{int}}.\Delta\sigma.B_\sigma(\sigma_k)}} \tag{19}$$

where $k \in \{0,\cdots,N-1\}$.

3.2 Study of a typical scenario

We will now compare the SNR given by the two types of architectures in a realistic scenario. Let us consider a gas plume appearing on a background (Fig.2a). The apparent spectral photonic radiance $L_{\sigma,sc}$ of the scene results from the contributions of the background and the gas. We assume that the background has a spectral photonic radiance $L_{\sigma,b}(\sigma)$ we assimilate to the spectral photonic radiance of a black body radiator (BBR) at the temperature T_b, which follows the photonic Planck's law $L_{\sigma,BBR}(\sigma,T_b) = 2c.\sigma^2/\left(\exp\left(hc\sigma/kT_b\right)-1\right)$. The gas, at the (assumedly uniform) temperature T_g, is essentially transparent in the studied wavelength range, except for absorption bands that lead to its specific spectral signature. If we denote $\tau(\sigma)$ the spectral transmittance of the gas integrated on the line of sight from the background to the instrument (and neglect all contribution from the atmosphere assumed to be perfectly transparent), the scene spectral luminance can be expressed as[8]:

$$L_{\sigma,sc}(\sigma) = \tau(\sigma).L_{\sigma,BBR}(\sigma,T_b) + (1-\tau(\sigma)).L_{\sigma,BBR}(\sigma,T_g)\,. \tag{20}$$

For the sake of simplicity, we assume that the gas presents only one *saturated* absorption line, that is, τ equals 0 for a particular wavenumber σ_g among the σ_k and increases rapidly to 1 on both sides, the underlying line width being greater than or of the order of $\Delta\sigma$ to be correctly seen by the instrument. Fig.2b shows the resulting scene spectral radiance.

As the saturated peak, depicted in light sky blue on Fig.2b, is the effective signal we want to detect, the effective radiance signal is no more the $L_{\sigma,sc}\left(\sigma_g\right)$ value itself but the peak height, which can be approximated for a small temperature difference by :

$$\Delta L_{\sigma,sc}\left(\sigma_g\right) = L_{\sigma,BBR}\left(\sigma_g,T_g\right) - L_{\sigma,BBR}\left(\sigma_g,T_b\right) \approx \frac{\partial L_{\sigma,BBR}\left(\sigma_g,T_b\right)}{\partial T}\Delta T\,. \tag{21}$$

where ΔT is the difference between gas and background temperatures $T_g - T_b$.

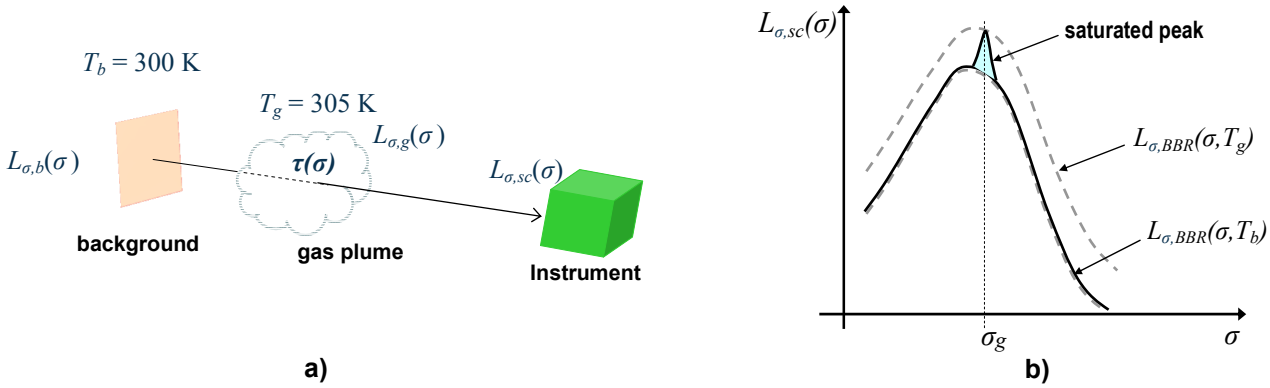

Figure 2: a) Scenario of the studied gas signature detection. b) Spectral radiance of the scene for our simplified model.

We can, thus, define, thanks to equations Eq.(2), and Eq.(17), a new "*useful signal* to noise ratio" by

$$SNR_{peak}(\sigma_g) = \frac{\Delta B_\sigma(\sigma_g)}{\sqrt{Var\left[\hat{B}_g\right]}} \tag{22}$$

where $\Delta B_\sigma(\sigma_g) = G.\tau_{lens}.\eta \times \Delta L_{\sigma,sc}(\sigma_g)$.

To give a numerical example, consider a scene observed in the two atmospheric windows 3-5µm and 8-12µm, with $\Delta T = 5$K and with a spectral resolution $\Delta\sigma$ of 5 cm^{-1}. Figure 3 represents the SNR (equation Eq.(22)) as a function of the peak wavenumber for the FT and direct methods. They have been computed with realistic incoming light and commercial sensor additive noise levels[9]. In the 8-12 µm range, even though the amount of incoming light is higher in the FT imager, the limited well capacity of present commercial sensor leads to reduce the integration time. The potential of the FT imager is not fully used and the SNR of the two methods are similar. On the other hand, in the 3-5µm range, the SNR appears slightly better for the FT-based imager. In this last case, the detector noise is dominant for the direct measurement method and the photon noise is dominant for FT method.

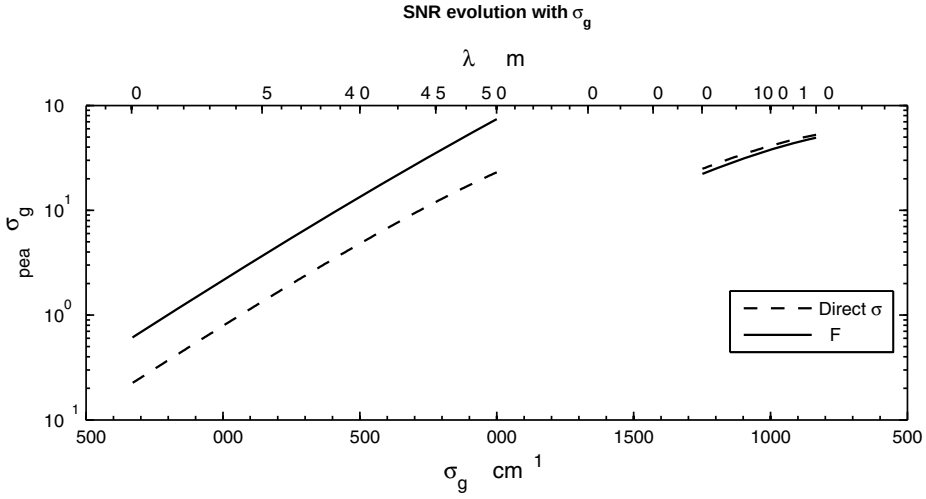

Figure 3: SNR defined as the ratio of the useful signal for a gas absorption peak detection to the noise standard deviation for the two methods under comparison: the direct acquisition of the spectrum and the Fourier transform on the two atmospheric windows 3-5 µm and 8-12 µm.

4. OPTICAL AND OPTO-MECHANICAL DESIGN OF THE INSTRUMENT

4.1 Aims and constraints for the design

The aim of the work was to build a simple proof-of-concept *laboratory* prototype in order to investigate practical implementation difficulties and show the effective material signature detection capability of such a spectro-imager. The prototype should be relatively easy to build with reasonable delay and cost. This led us to mostly use available components in our lab or on-the-shelf commercial components. Especially, the right angled hollow roof mirrors assemblies should be 1 or 2 inches wide (hypotenuse length) and the semireflecting plate and compensator plate smaller than 3 inches for their larger dimension.

A CEDIP JADE 77K-cooled MWIR camera built upon a 320×240 detector array with 30µm pitch was available. The defined choice of the detector array immediately determines the ultimate spectral resolution that can be reached, as the Shannon sampling theorem implies that less than 320/2 = 160 fringes at the lower wavelength of the spectral range should be imaged across its larger dimension. The optical path difference (OPD) excursion over the whole field of view (FOV) of the imaging interferometer, δ_M , may be expressed as

$$\delta_M = t.\sin(\theta_{½}) - t.\sin(-\theta_{½}) = 2\times t.\sin(\theta_{½}). \tag{23}$$

where $\theta_{½}$ is the maximum half FOV in the largest sensor direction (cf. Fig.1 and Eq.(3)). The above-mentioned limited fringe number implies that δ_M is less than 160×3.0µm = 0.48mm for the 3-5µm spectral range of interest. If we do not make use of the theoretical symmetry of the interferogram with respect to the zero OPD, FT spectroscopy thus leads to a wavenumber sampling step $\Delta\sigma = 1/\delta_M$ greater than 1/0.48mm ≈ 21cm^{-1}. We will use in practice a wavenumber sampling step $\Delta\sigma$ near ~25cm^{-1}, adequate for the aforementioned targeted application, which yields ~130 fringes at 3µm or ~100 fringes at 4µm over the whole field of the imaging interferometer. This spectral resolution is implemented by adjusting the lateral translation $t/2$ of one of the roof mirrors with respect to the image of the other through the beamsplitter *(cf. Fig.1)* to

$$t/2 = \frac{1}{4.\Delta\sigma.\sin(\theta_{½})} \tag{24}$$

(For example, for $\theta_{½}$ = 2.75°, $\Delta\sigma$ = 25cm^{-1} leads to $t/2$ near ~2.1mm, an easily accessible value).

4.2 Influence of parameters and design choices on the interferometer size

Since the interferogram of a given scene point builds up as its image crosses the field in a pushbroom-like acquisition mode, as explained §2, uniformity of the response over the field is of concern. Even though radiometric dome correction can be carried out in the context of non uniformity correction (NUC) of the detector array, geometrical vignetting should be avoided over the whole field of view of the instrument, as it might not only deteriorate the signal level but also distort the spectrum if it is not achromatic. Therefore, the size of the interferometer components, roof mirrors and semireflecting and compensating plates, should be sufficient to avoid any ray clipping. This implies that the interferometer size will strongly depend of the beam étendue, i.e. the entrance pupil diameter (EPD) and the FOV, but also on the axial position of the entrance pupil of the lens, as shown in Fig.4.

It is easy to understand that the interferometer footprint will be minimized for a given FOV and EPD when the entrance pupil is positioned in the 'middle' of the interferometer, that is on the roof mirror ridge, the beam splitter being hit two times by the ray, before and after the reflection on the roof mirrors. This means that the lens entrance pupil should be *real* some distance *ahead* of its first glass. However most standard lenses have usually a *virtual* entrance pupil positioned *behind* its first glass. Fortunately, some kinds of objectives designed for use with a scanning mirror have an appropriately placed pupil.

4.3 Actual design of interferometer and lens

As the image size is already given by the pitch and the number of pixels of the detector array, namely 9.6mm × 7.2mm for our JADE CEDIP camera sensor, the focal length of the imaging lens is determined by the FOV. For a specific application, like airborne remote sensing, the EPD and FOV would have been established by a trade-off between

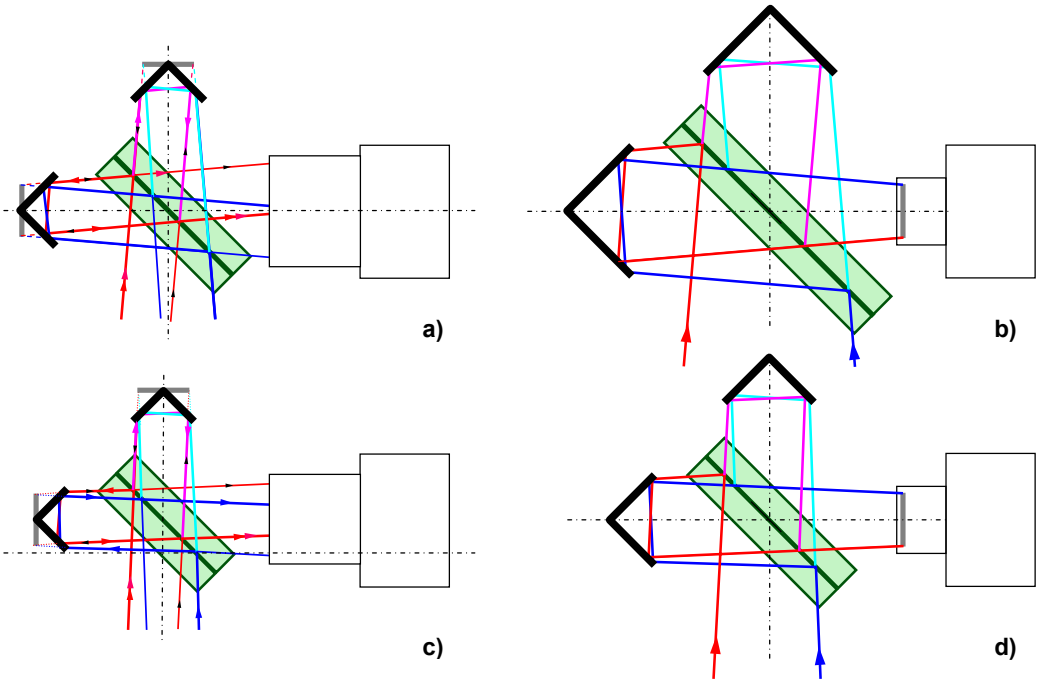

Figure 4: Schematic diagrams showing the effect of pupil position and FOV on the interferometer size for a given EPD. *(All four sub-figures are drawn at the same scale).* The green 45° double-rectangles depict the splitter and compensator plates, and the thick gray segments the entrance pupil of the imaging lens.
a)&c): best position (on the roof mirrors ridge) for the lens entrance pupil. b)&d): standard virtual entrance pupil inside the lens. a)&b): 10° (±5°) FOV c)&d): 5° (±2.5°) FOV

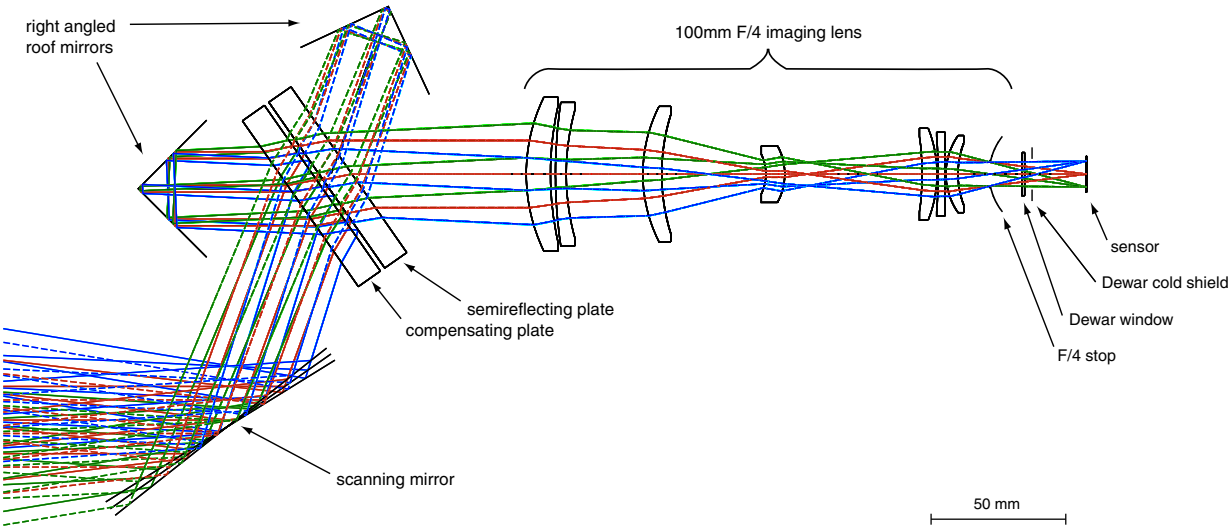

Figure 5: Complete set-up of our FT imaging spectrometer with a 100mm F/4 lens (±2.75° FOV), a right angled roof mirrors Michelson interferometer with a 35° tilted beam-splitter assembly, and a scanning mirror needed to introduce the requested pushbroom behavior on a laboratory instrument. The detail of the vacuum cooled Dewar housing of the sensor (window, cold shield, ...) and external F/4 stop is shown on the right.

radiometric considerations and operational specifications. In our case, for a laboratory demonstration instrument, we choose the best available lens that fulfills the constraints detailed in sub-section 4.2. We used a *Thales Optronique SA* 100mm F/2.65 imaging lens fitted for our cooled sensor with its Dewar cold shield, that exhibits a real 'aerial' entrance pupil 135mm ahead of the first glass with excellent aberration correction (diffraction limited) over the whole FOV (±2.75°×±2.06°). Nevertheless, we had to close down the lens to F/4 (25mm EPD) and to straighten up the beam-splitter from 45° to 35° to keep the beamsplitter and compensating plates clear aperture size below 70mm, provisioning for mechanical mounts and for some positioning error budget on 3" plates.

4.4 The "DéSI²R" instrument

Thanks to the LCF-IO mechanical shop, the opto-mechanical mounts for the interferometer, lens and camera were designed and fabricated. Fig.6 shows a picture of the instrument, which we named "DéSI²R" for the French «**Dé**monstrateur de **S**pectro-**I**mageur **I**nfra-**R**ouge» *(Infra-red spectral imager demonstrator)*.

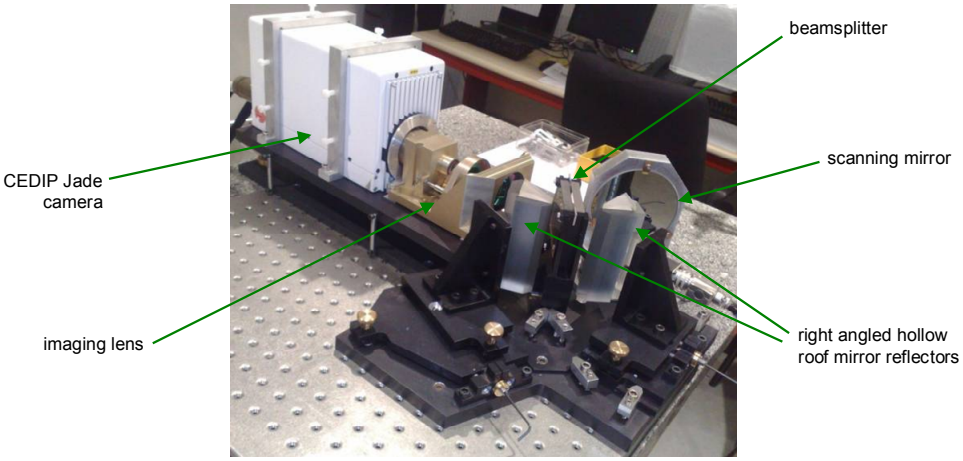

Figure 6 : Picture of the "DéSI²R" instrument in our lab.

The next paragraph presents the first results obtained with this instrument.

5. PRELIMINARY RESULTS

As a first test, we tried to study material signature detection. As experiments on true gases would have required complex facilities and protocols, we instead choose to work with easy-to-use commercial *polyethylene* film, which presents a strong and complex absorption band in the vicinity of 2900cm^{-1} (~3.45µm) inside the 3-5µm (2000-3300cm^{-1}) spectral range as shown in Fig.7.

5.1 Non imaging spectrometer mode

The first tests on the DéSI²R instrument have been conducted with a simple ***non*** *imaging* acquisition procedure, where a (more or less uniform) source is placed as close as possible of the instrument entrance pupil, instead of being positioned at infinity or at a large distance relative to the focal length of the lens (Fig.8a). This leads to observing fringe modulation on a uniform scene after applying a sensor NUC (Fig 8b), as in conventional *static* FT spectrometers. Therefore a simple Fourier Transform of the acquired image gives the spectrum of the 'global' source without the need to scan the scene and process the image stack with tricky image registration and scene point interferogram extraction algorithms. The source was either a 'naked' BBR with a 10cm×10cm emitting area at temperature T_{BBR} adjustable between 10°C and 60°C, or the same BBR in front of the instrument with a polyethylene sheet nearly at ambient temperature inserted between the source and the interferometer front element (Fig.8a).

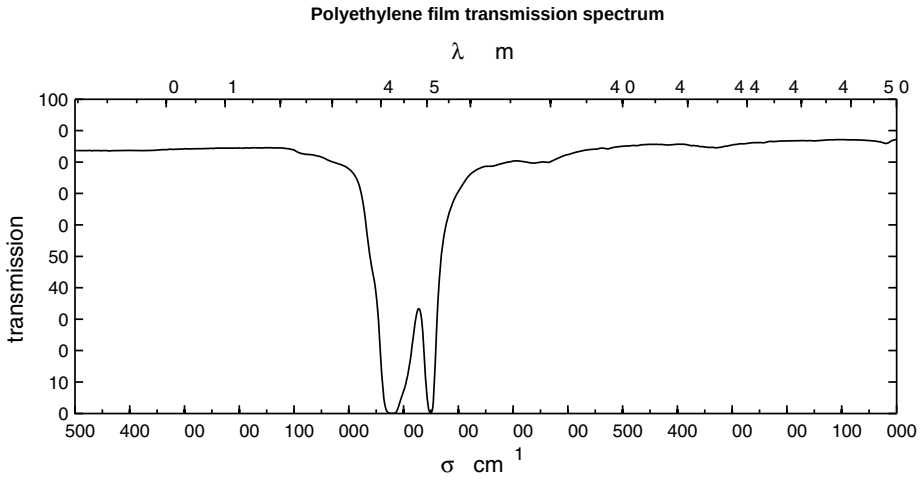

Figure 7 : Polyethylene film transmission spectrum measured between 2000 and 3500cm^{-1} with a Perkin-Elmer FTIR spectrometer (1cm^{-1} sampling, ~4cm^{-1} spectral resolution). Two strong absorption bands at respectively ~2920cm^{-1} and ~2850cm^{-1} are clearly visible. (The second band is somewhat narrow with respect to the ~25cm^{-1} spectral resolution $\Delta\sigma$ of the DéSI²R instrument)

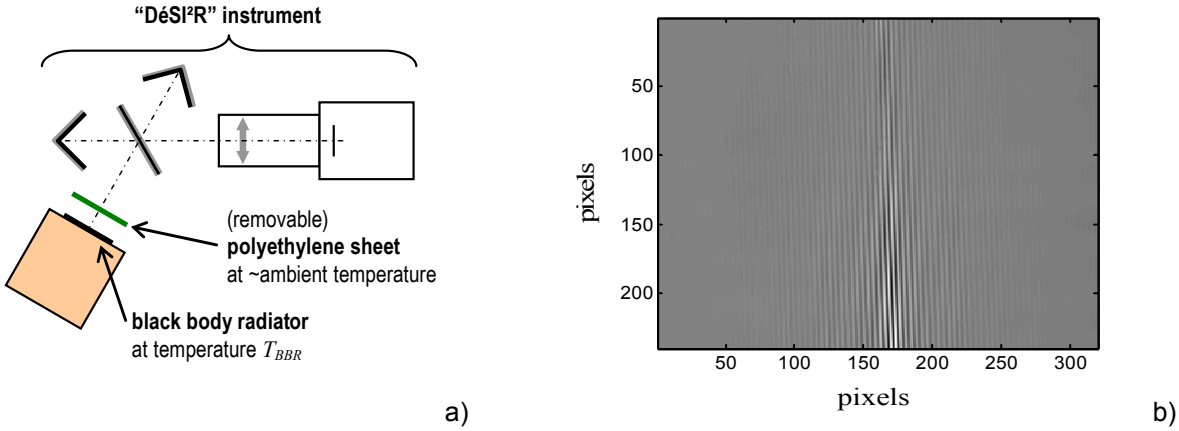

Figure 8 : Non imaging spectrometer mode: a) the experimental set-up b) Acquired image for a BBR at 50°C filtered by a polyethylene film at nearly ambient temperature (~23°C) *(A detector array NUC has been applied)*. The slightly slanted tightly packed fringes with decreasing contrast from the 0 order fringe can be readily seen. *(Slight artifact Moiré effects appear in the figure as the fringe spatial frequency is close to the sensor Nyquist frequency)*

The fringes were slightly slanted with respect to the rectangular sensor sides in order to reduce side-effect artifacts in the spectrum computation by 2D FFT. In order to improve the SNR, we in fact averaged results over 900 similar images. Our results for the naked BBR at 30°C and 50°C and the polyethylene sheet at ambient temperature in front of a 50°C BBR are given in Fig.9. The polyethylene absorption band around 2920cm^{-1} is clearly visible; the not fully resolved 2850cm^{-1} band may also be probably noticed as an inflexion point in the curve.

5.2 Preliminary spectral image acquisitions

The next step was to acquire true spectral images of a scene. This necessarily involves the scanning of the scene and large processing amounts on the interferometer image stack. For this first attempts, we used minimally modified algorithms previously developed for our former work on a visible FT imaging spectrometer "CaHyD"[6][7]. The main

object in the scene was a BBR at temperature T_{BBR} seen by reflection on a mirror at ambient temperature T_{amb}, about half of which had been covered by a polyethylene film (Fig.10). The rest of the scene was intentionally temperature textured by heated electric resistors randomly positioned on a plate in order to let the image stack registration algorithm work all over the acquisition scanning. This scene was placed at ~3.2m of the DéSI²R scanning mirror, the maximum distance that can presently be achieved in our lab (Fig.10). This distance is too short for our 100mm F/4 lens to allow correct focusing of the scene simultaneously with the infinity located fringes and no IR supplementary lens with the appropriate focal length was available yet to bring the scene back to focus. As we chose to favor fringe sharpness, the scene details were blurred, but that did not affect the ability to see a spectral signature on two small uniform areas on the left and right zones of the BBR image, one with and the other without filtering by the polyethylene film.

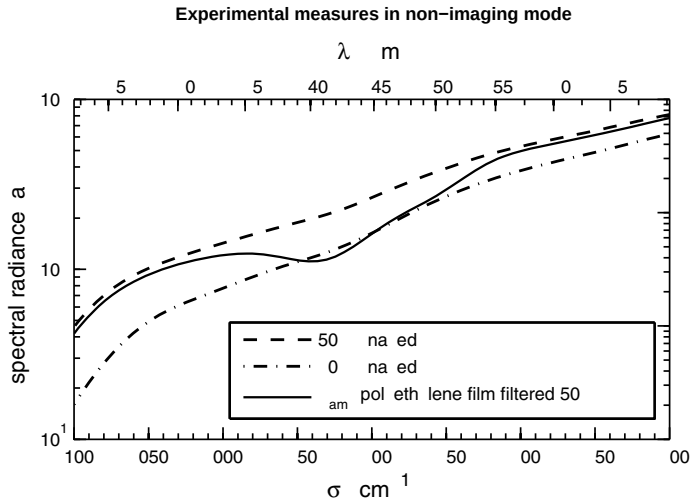

Figure 9: Spectra obtained in non imaging spectrometer mode on the vicinity of the polyethylene absorption band region. (The experimental spectral resolution is ~26cm^{-1}. *Zero padding used in the FFT computations leads to a four times smaller σ sampling that smooths the curve but does not increase the resolution.*)

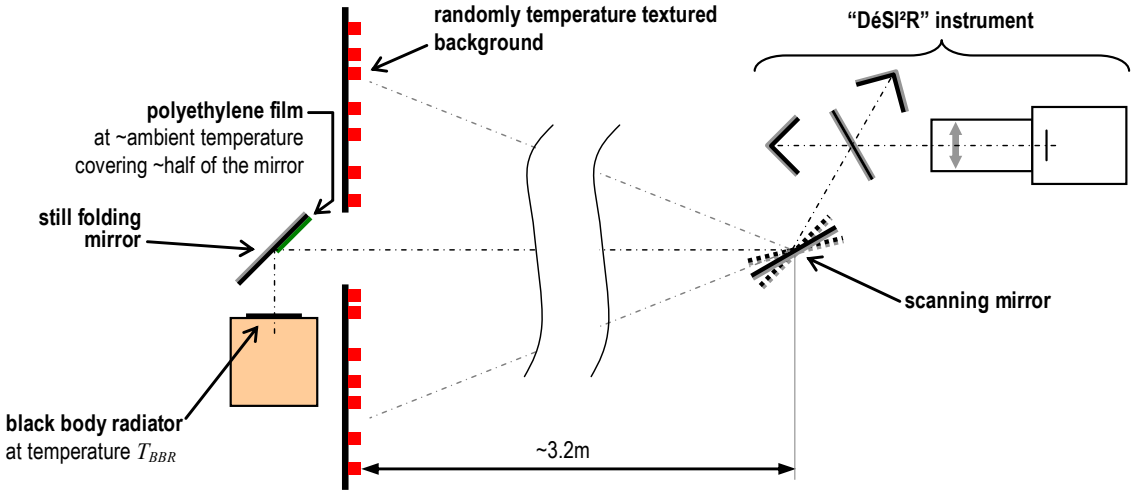

Figure 10: Experimental setup for "spectral imager" mode

One image from an acquisition sequence is shown Fig.11a. Results of spectral image computation from raw image stacks are given Fig.11b and Fig.12. The polyethylene signature is clearly visible from the Fig.11b curves. It is of course

impractical to display the whole 3D computed spectral image cube. For Fig.12, we selected three particular wavelengths (2795cm^{-1} or 3.58µm, 2917cm^{-1} or 3.43µm and 3040cm^{-1} or 3.29µm) and depicted the spectral image intensity in these channels in red, green and blue respectively. The middle wavelength was chosen to be on the deeper part of the polyethylene absorption band. Fig.12b and 12d clearly show the two adjacent zones of the BBR image, with ambient temperature polyethylene film filtering on the left, and no filtering on the right.

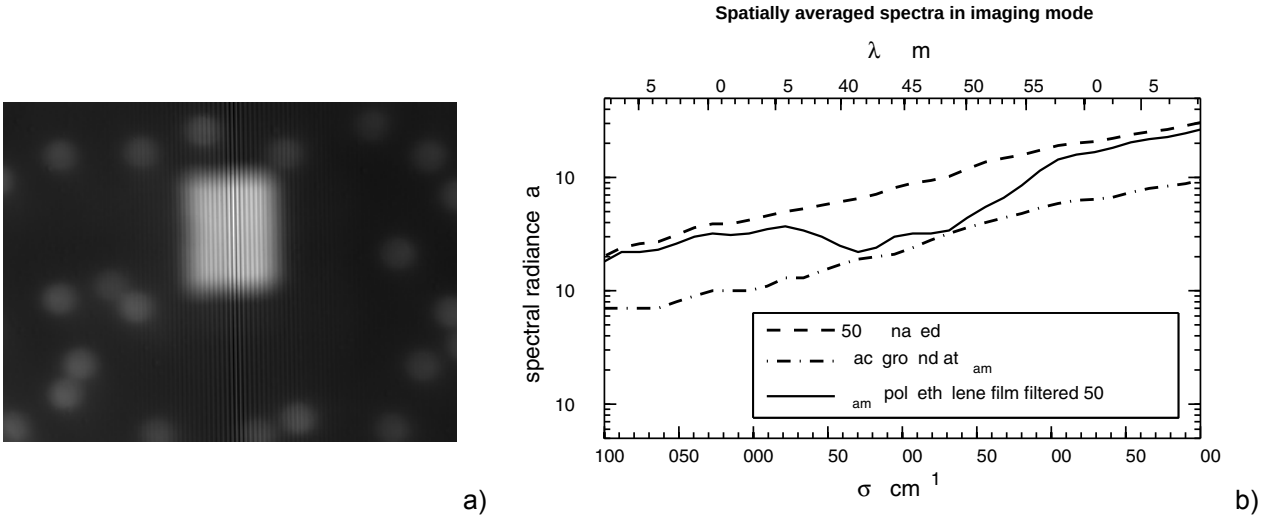

Figure 11: preliminary spectral imaging mode results for a scene formerly described in text and Fig.10. a) One image (with NUC) of the acquired interferogram image raw stack. The light gray rectangle in the center is the image of the 50°C BBR. The left part of the BBR image is filtered by the ambient temperature polyethylene film; The random gray dots on a black background are the (blurred) images of the heated resistors. b) Average spectrum of small zones of the background and of the polyethylene film filtered and unfiltered BBR in the vicinity of the polyethylene spectral absorption bands around ~2920cm^{-1} and ~2850cm^{-1}.

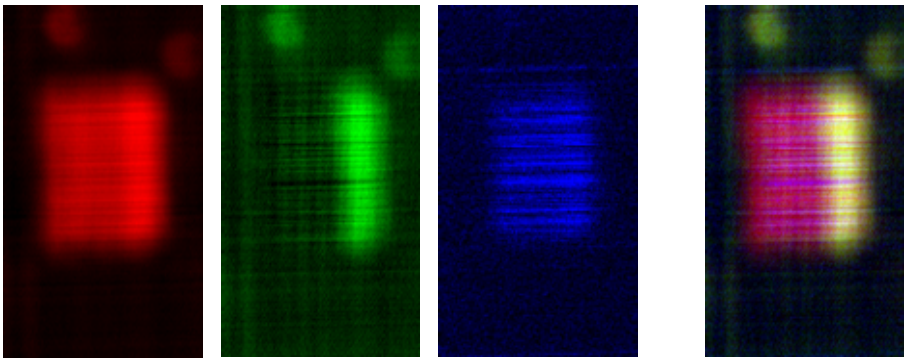

Figure 12 *(color in electronic version)*: False color images of the BBR taken from three particular channels of the whole 3D computed spectral image of the scene:
a): *Red:* 2795cm^{-1} or 3.58µm. b): *Green:* 2917cm^{-1} or 3.43µm c): *Blue:* 3040cm^{-1} or 3.29µm.
d): composite RGB image of the three channels.

6. CONCLUSION

We have reported the theoretical analysis, the design and the preliminary experimental results of a FT-based imaging spectrometer in the 3-5µm wavelength range. We built a cost-limited laboratory demonstrator that avoids any vignetting while keeping the size of the interferometer component as low as possible. We present clear evidence for polyethylene

film signature detection, either in non imaging and imaging acquisition modes, with design spectral resolution ~25cm^{-1}, appropriate for a large number of targeted applications. Further experimental investigations will focus on spectral and radiometric calibration issues. The aim will be to measure the experimental SNR in specific situations and correlate it with the theoretical noise models presented in the first part of this paper, in order to check the soundness of such modeling.

REFERENCES

[1] Inoue T., Itoh K. and Ichioka Y., "Signal-to-noise ratio of Fourier-transform spectral imaging in the image plane and pupil plane",Optik, Vol.98(4), 175 - 180 (1995).

[2] Bergstrom D., Renhorn I., Svensson T., Persson R., Hallberg T., Lindell R. and Boreman G., "Noise properties of a corner-cube Michelson interferometer LWIR hyperspectral imager", Proc. SPIE 7660, 76602F 1-8 (2010).

[3] Cabib D., Gil A., Lavi M., Buckwald R. A., and Lipson S. G., "New 3-5 µm wavelength range hyperspectral imager for ground and airborne use based on a single-element interferometer", Proc. SPIE 6737, (2007).

[4] Ferrec Y., "Spectro-imageurs", Techniques de l'ingénieur, E4111, (2010).

[5] Ferrec Y., Taboury J., Sauer H. and Chavel P., "Compactness of lateral shearing interferometers", *to be published in* Appl.Opt., (accepted June 2011).

[6] Ferrec Y., *PhD thesis*, "Spectro-imagerie aéroportée par transformée de Fourier avec un interféromètre à décalage latéral : réalisation et mise en œuvre", Université Paris Sud 11, Orsay, France, (2008).

[7] Ferrec Y., Taboury J., Fournet P., Sauer H., Goudail F., Chavel P., Guérineau N., Coudrain C., Thétas S., Cymbalista P., Primot J., and Deschamps J., " Design of a Fourier-Transform Spectral Imager for Airborne Measurements", in *Fourier Transform Spectroscopy/ Hyperspectral Imaging and Sounding of the Environment*, OSA Technical Digest Series, paper FThB3, (2007) .

[8] Boyd R.W., [Radiometry and the detection of optical radiation], John Wiley and Sons, New York, (1983).

[9] Ayari-Matallah N., *PhD thesis*, "Imagerie hyperspectrale par transformée de Fourier – Limites de détection, caractérisation des images et nouveaux concepts d'imagerie", Université Paris Sud 11, Orsay, France, (2011).